Revisiting dispersion and reactivity of active sites via a restricted random distribution model over supported vanadia catalysts for NO reduction

Jingyu Xue [a], Yang Zhang [b], Wenshuo Hu [c], Yanrong Chen [a], Zhongqing Yang [a], Jingyu Ran [a], Xinbao Li [d], Xin Tu [e], Xuesen Du [a,*]

[a] *Key Laboratory of Low-grade Energy Utilization Technologies & Systems of Ministry of Education of China, School of Energy and Power Engineering, Chongqing University, Chongqing 400044, China*

[b] *Huadian Electric Power Research Institute Co., LTD, Hangzhou 310030, China*

[c] *State Key Laboratory of Clean Energy Utilization, Zhejiang University, Hangzhou 310027, China*

[d] *Faculty of Maritime and Transportation, Ningbo University, Ningbo 315211, China*

[e] *Department of Electrical Engineering and Electronics, University of Liverpool, Liverpool L69 3GJ, UK*

*Corresponding author. *E-mail address:* xuesendu@cqu.edu.cn (X. Du).

ABSTRACT: The structure and dispersion of active sites substantially impact the performance of supported metal oxide catalysts, as exemplified by the V_2O_5/TiO_2 catalysts used for NH_3-SCR reaction. Due to the complexity of the active site dispersion on the catalyst surface, the intrinsic law of this structure–activity relationship remains controversial. Herein, we proposed a restricted random distribution model to describe the stochastic anchoring behavior of active sites on the TiO_2 surface during the loading process of vanadia. The structures of monomeric, dimeric, and polymeric VO_x sites were determined by DFT calculations and verified with spectroscopy and adsorption information experimentally. The calculated reaction pathways and energy profiles for these structures indicated that the dual sites configuration and terminal $V(=O)_2$ bond are responsible for the high reactivity of aggregated VO_x sites. Combining the reactivity of these various sites and the random distribution method, we built a general profile of the correlation between the V_2O_5/TiO_2 catalyst surface and its reaction performance. The reactivity results obtained from experimental *in situ* DRIFTS and kinetic tests validate our theoretical model. The

random distribution method links DFT calculations and experiments, coupling the structure and dispersion of the VO_x active sites to the catalyst reactivity.

***Keywords*:** Supported catalysts, Selective catalytic reduction, Vanadium oxides, Active sites, Reaction mechanisms

1. Introduction

For supported heterogeneous catalysts, the catalytic activity depends significantly on the interaction between the active sites and the support [1–3]. The V_2O_5/TiO_2-based catalysts are a typical example of catalysts with such dependence on metal oxide-metal oxide interaction. These catalysts have been widely utilized in many important reactions, such as selective oxidation of alkanes and alcohols, oxidation of SO_2 for H_2SO_4 production, selective reduction of NO_x with NH_3 (SCR), and other upcoming reactions [4–8]. Due to the complexity of V_2O_5 distribution on the TiO_2 surface and the related coordination behaviors, the reaction mechanism remains in debate. A massive amount of research interest has been put into studying this catalyst system. Raman [9–14], NMR [15–17], and Exafs [18–21] were applied to characterize the coordinating environment of VO_x on the TiO_2 surface. A consensus has been reached that both monomeric and polymeric vanadia species exist in V_2O_5/TiO_2 catalyst and that the percentage of these two species will change upon increasing the vanadia loading. The molecular structure of monomeric vanadia is much clearer than that of polymeric. A tetrahedral VO_4 structure with one short V=O bond and three moderate V−O bonds is believed to be the dominant species of monomeric vanadia lying on the TiO_2 surface. Raman and NMR results are all supporting this hypothesis [12,16]. The monomeric vanadia site has also been widely used for theoretical calculations [22–25]. However, the structure of polymeric vanadia has gained much less attention, although it has been proved to be times more active than monomeric one. The information on the structure of polymeric vanadia is somewhat limited. Through Raman characterization, the broad peak around 930 cm^{-1} was assigned to the Raman vibration of polymeric vanadia [10–12]. The structure of polymeric VO_x

45 species can be further characterized via correlating the experimental NMR spectra and theoretical NMR chemical
46 shifts [16]. He et al. [26] modeled a vanadia dimer on a TiO_2 (101) surface and calculated the reaction paths to
47 compare the energy profiles of SCR reactions over monomeric and polymeric vanadia sites.

48 Regarding the complexity of the reactive site on the V_2O_5/TiO_2 catalyst, numerous mechanisms have been
49 proposed for one specific reaction, such as the SCR reaction. Lewis acid was believed to be formed in V_2O_5/TiO_2
50 catalyst and play a decisive role in the SCR reaction [27]. While in other views, Brønsted acid (V^{5+}−OH) and the
51 V=O site are needed [28,29]. Zhu et al. [30,31] compared the reaction rate of L and B acid sites and concluded
52 that L acid is more active than B acid. They also proposed that the reoxidation of V^{4+} is significantly faster than
53 the reduction half cycle. Theoretical calculations based on DFT have been an essential supplement for studying
54 the SCR mechanism on V_2O_5/TiO_2 catalyst [24,26,32], since the reaction information achieved from experiments
55 is still limited. Based on the discussion of the above complexity, we suggest that the intrinsic correlation between
56 the structure, dispersion, and reactivity of the active sites over V_2O_5/TiO_2 catalysts has not been identified clearly.

57 In the present study, we aimed to build a general profile of the V_2O_5/TiO_2 catalyst surface and provide a solution
58 to link the surface structure with the catalyst reactivity. We elucidated the clear relationship between the active site
59 structure and SCR reactivity on V_2O_5/TiO_2 catalyst using periodical DFT calculations combined with experiments.
60 Based on the formation energies from DFT calculations, the most stable monomeric, dimeric, and polymeric VO_x
61 structures were screened out as target sites and verified with Raman spectra and NH_3-TPD information. A restricted
62 random distribution model of VO_x sites was established to describe the variation of active sites morphology and
63 quantity with vanadia loading, acting as a bridge between DFT calculations and experiments. The detailed reaction
64 pathways with structure and energy profiles were calculated, with a focus on rate-controlled energy barriers as
65 determinants of reactivity. A series of experiments, including *in situ* DRIFTS and kinetic tests, were employed to
66 demonstrate the variation in reactivity of the different active sites. The computational activation energy was

calculated combined with the random distribution model. It was used to compare with the experimental activation energy, thus validating the theoretical model in this study.

2. Experimental and computational methods

2.1. Catalyst preparation

In this work, the V_2O_5/TiO_2 samples with different V_2O_5 loadings (0.5 wt.%–5 wt.%) were prepared by conventional incipient wetness impregnation, denoted as *x*V/Ti (*x*=0.5,1,2,3,4,5). Commercial TiO_2 powder (P25, Degussa) with a surface area of 55.3 m^2/g was used as support material. According to the loading of vanadia, a certain amount of ammonium metavanadate (NH_3VO_3, 99.9%, Aladdin) was dissolved in oxalic acid ($C_2H_2O_4$, 99%, Aladdin) to form the precursor solution. The precursor solution and TiO_2 powder were mixed by mechanical stirring and oscillated in an ultrasonic oscillator for 30 min. Subsequently, the obtained mixture was dried overnight in an oven at 110 °C and calcined at 500 °C for 5 hours in air condition. The general properties of the V/Ti samples are presented in Table S1. In addition, the XRD patterns show that the V_2O_5 crystals did not appear in all samples, proving good vanadia dispersion (Fig. S1).

2.2. Catalyst activity test

The NH_3-SCR activity test of the V_2O_5/TiO_2 catalyst was implemented in a fixed-bed quartz tube reactor with an internal diameter of 7 mm. A certain mass of catalyst sample with 40–60 mesh was filled in the reactor for the test. The feed gas mixture consists of 500 ppm NH_3 (2% NH_3/N_2, Chongqing Ruike), 500 ppm NO (2% NO/N_2, Chongqing Ruike), 5% O_2 (99.999%, Chongqing Ruike), and N_2 (99.999%, Chongqing Ruike) as balance gas. The total gas flow rate was set to 2 L/min. The reaction was performed based on dry conditions (without extra water). Protea ProtIR 204 infrared gas analyzer was used to measure the NO concentration. The conversion (X_{NO}) and reaction rate (v_{NO}) of NO were obtained by measuring the change in NO concentration before and after the reaction,

as well as the gas flow rate (Eqs. S1 and S2). TOF (Turnover frequency) can indicate the intrinsic activity of the active site, which was calculated as follow:

$$TOF(s^{-1}) = \frac{v_{NO}}{N_{V\text{-}site}} \quad (1)$$

where v_{NO} (mol/(g.s)) is the reaction rate of NO, and $N_{V\text{-}site}$ (mol/g) is the number of vanadia sites on the catalyst surface. The conversion rate was kept below 30% to ensure the reactor differential assumption and thus the accuracy of the TOF calculation. The mass of the catalyst was set to keep the molar amount of vanadium constant (shown in Fig. S2).

2.3. Catalyst characterization

Raman spectra were measured on an Andor SR-500i spectrometer using a 532-nm laser excitation source. The spectrometer was equipped with an *in situ* reaction cell, where samples can be heated in a gas flow. In our experiments, in order to ensure complete oxidation of catalysts, all samples were heated to 400 °C under oxygen flow, and then the Raman spectra were acquired.

In situ DRIFTS analysis was carried out using a PerkinElmer Spectrum 3 spectrometer with an MCT detector. A background spectrum in an N_2 flow was sampled before each experiment. All the IR spectra were obtained by collecting 64 scans with a resolution of 4 cm^{-1}.

NH_3-temperature programmed desorption (NH_3-TPD) of the V_2O_5/TiO_2 catalysts was operated on a dynamic sorption analyzer with a thermal conductivity detector (TCD). After being pretreated in N_2 atmosphere at 400 °C for 1 hour, 0.2 g catalyst was treated in the NH_3-contained atmosphere (1.2% NH_3 and N_2 as balance, the total flow rate is 50 mL/min) for 1 hour at 100 °C for NH_3 adsorption. Then the catalyst was treated by N_2 purge at 100 °C for 1 hour. Finally, the catalyst was heated from 100 °C–500 °C at 10 °C/min.

Details of other characterization methods were mentioned in the supporting information.

2.4. Computational details

In this study, all periodical calculations based on density functional theory (DFT) were implemented in the Vienna ab initio simulation package (VASP), using Perdew–Burke–Ernzerhof generalized gradient approximation (PBE-GGA) functional [33] with vdW correction by DFT-D3 approach [34]. The Hubbard U was applied to Ti 3d and V 3d state (U_{eff} = 3.5 eV) to correct the electron localization [35,36]. The reliability of the PBE + U/D3 functional can be verified by comparing it with a more accurate functional (detail in Table S2). Spin-polarization was considered for unpaired electrons. The cut-off energy of the plane wave was set to 400 eV. Gaussian smearing was used with the width setting to 0.1 eV. The structures were considered to be optimized when the force was less than 0.03 eV/$Å^{-1}$ and the break condition for the electronic SCF-loop was set to 10^{-5} eV. Only the Γ point of the Brillouin zone was sampled [26]. Transition states (TS) were obtained by climbing image nudged elastic band (CI-NEB) method in Transition State Tools for VASP (VTST) [37]. Harmonic vibrational frequencies were calculated by the finite-difference method. The free energies were calculated involving zero-point energy corrections and vibrational entropy within the harmonic approximation (gas molecules involve gas-phase entropy). The cluster-based calculation of the Raman spectra was carried out using the Gaussian 09 module at the B3LYP/6-31(D, P) level.

For matching the P25 TiO_2 support (anatase accounts for 79% [38], composed mainly of thermodynamically stable (101) surface) in the experiment, the anatase (101) surface model was selected in the DFT calculation in this work (the XRD and TEM results are shown as support in Figs. S1 and S3). The anatase crystal and a (2×3) supercell of the anatase (101) surface were constructed and optimized, as shown in Fig. S4. The lattice parameters and the surface energy of the optimized models agreed well with the data in the previous literatures [39,40].

The restricted random distribution model of activity sites was implemented via the NumPy module from python. In the distribution model, a two-dimensional array of 100×100 size was used to represent the locations of 10,000

Ti_{5c} sites on the TiO_2 (101) surface. These locations will be gradually occupied by V active sites at random. According to the lattice parameters of the TiO_2 (101) surface in DFT calculation and the specific surface area (55.3 m^2/g) of the TiO_2 support in the experiment, the numbers of Ti_{5c} and V sites on the catalyst surface per unit mass can be obtained. And then, the random distribution model can be connected with the real catalyst in terms of the number of sites (Table S3).

3. Results and discussion

3.1. Structure of VO_x active sites on TiO_2 surface

Finding the most stable structures of vanadium oxide (VO_x) on a substrate in different loadings conditions is challenging. In this study, the VO_x loading method was applied, which can be described as the process of a specific monomeric VO_x species being sequentially anchored. Here, a VO_3H (Fig. S5A) unit was regarded as the rational unit structure for anchoring. The formation energy of the VO_3H unit on the substrate was used to assess the stability of different structures of VO_x species, which was defined as Eq. S4.

The possible anchoring configurations of VO_3H were suggested in the case of sufficient Ti sites (two adjacent Ti_{5c} sites are available at least), as shown in Fig. S5B. One or two Ti_{5c} sites and one O_{2c} site were employed to bind to VO_3H in these structures. The O_{2c} site assisted the formation of the VO_3H tetrahedral coordination structure. It can be seen that the most stable configuration is 1a (Fig. S5B), with the largest formation energy. In this condition, two Ti_{5c} and one O_{2c} were occupied by the VO_3H, and −OH was located between the V and Ti atoms. Here, we defined this as a typical monomeric VO_x configuration (denoted as Monomer), which dominants at low vanadia loading. Then, with the increase of vanadia loading, the amount of exposed Ti atoms decreased and it was assumed that there would be only one exposed Ti_{5c} site, or even no Ti_{5c} site, within a specific range. For the former case, the VO_3H would bind to the exposed Ti_{5c} next to an existing Monomer (Fig. S5C, two VO_3H involved). The formation energy of the horizontal structure (2a) is greater than that of the vertical one (2b). For the latter case, the

VO_3H would locate on two anchored Monomers (Fig. S5D, three VO_3H involved). The vertical structure (3a) is more stable than the horizontal one (3b). The above formation energies were summarized in Fig. S5E that the structure of VO_3H bound to two Ti_{5c} sites is the most stable. This indicates that the VO_3H loading on the TiO_2 surface tends to form Monomer preferentially, which can guide the anchoring order of VO_3H during the loading process. However, the supported VO_x phase was believed to exist in a relatively dehydrated state under SCR reaction condition [11]. Thus, we considered the VO_3H units (2a and 3a in Fig. S5E) to form dimeric or polymeric configurations via dehydration. The phase diagrams of thermodynamic analysis were employed to identify the dehydration states of the VO_x structure under different conditions. The free energy difference between the states of dehydration and hydration was calculated according to Eqs. S5 and S6. The phase diagrams and the corresponding configurations before and after dehydration are shown in Figs. S5F and S5G. It can be seen that both kinds of VO_x exhibit a dehydrated state both in the calcination condition (773 K, 1% H_2O) and in most cases of the SCR reaction condition (473 K~723 K, < 500 ppm H_2O). Therefore, the above two dehydrated VO_x configurations were selected as the research objects (denoted as Dimer and Polymer) for higher V_2O_5 loading conditions.

The structures of Monomer, Dimer, and Polymer were determined based on the above calculations, as shown in Figs. 1A and S6 in detail. They all present with tetrahedral coordination. Since the configurations only involve the dehydration between VO_3H, the valence states of vanadium atoms are all considered +5 (see Table S4 for the Bede charge results for the V atoms). It can be seen that Monomer and Dimer both contain single terminal oxygen (V=O) with a bond length of 1.60 Å. Notably, a unique double terminal oxygen (O=V=O) structure appeared in Polymer, whose bond length is extended to 1.61–1.63 Å. The remaining V−O single bonds have lengths between 1.70–1.99 Å according to different coordination conditions.

Moreover, a restricted random distribution model was built to predict the quantitative changes of the three VO_x configurations in the sequential anchoring process. It was based on the assumption that the loading of V sites during the catalyst preparation is stochastic. In this process, VO_3H units randomly appeared on a certain Ti_{5c} site in turn. They were converted into the Monomer, Dimer, or Polymer according to the priority order determined by the formation energy. It can be referred to as a restricted random distribution process. Fig. 1B is the schematic diagram of a more extensive size range of TiO_2 (101). Within a specific range, when the exposed Ti_{5c} sites are sufficient, the Monomer is formed preferentially. Only when Ti_{5c} sites are insufficient or absent will the Dimer and Polymer be formed on the Monomer base sequentially. As shown in Fig. 1B, the green triangles represent the Monomer that has been formed, and the blue triangles (noted in M, D, and P) indicate the formation and order of the Monomer, Dimer, and Polymer under certain conditions. Fig. 1C demonstrates the changes in the number of the Monomer, Dimer, and Polymer with the increase in V_2O_5 loading. Among them, the number of Polymers was indicated by that of V with double-terminal oxygen. Due to the priority of Monomer formation, when the V_2O_5 loading is lower (<1.5 wt.%, ~1.8 V/nm^2), the number of Monomers increases gradually and takes absolute advantage. Then as the loading of V_2O_5 continued to increase (>1.5 wt.%, ~1.8 V/nm^2), the Dimer and Polymer were gradually formed based on Monomer through dehydration, resulting in a decrease in the number of Monomers. The increase in the number of Polymers is greater than that of Dimers, and gradually the Polymer becomes dominant in number. When the loading of V_2O_5 reaches about 3.5 wt.% (~4.3 V/nm^2), all Ti_{5c} sites and hydroxyl groups of Monomers are consumed, causing no more VO_3H can be anchored. We assumed that before reaching the theoretical monolayer coverage of V_2O_5/TiO_2 (~8 V/nm^2) [7], the VO_x species with a higher degree of polymerization would be formed based on the existing Polymer, or even V_2O_5 crystallization. These contents are beyond the scope of this study.

To verify the rationality of the configurations and the random distribution model, Raman spectra obtained by experiment and DFT calculation were applied to identify the feature of VO_x structures, as shown in Figs. 1D and 1E. Two characteristic bands at 1030 and 930 cm^{-1} were observed in the experimental Raman spectra, which belong to monomeric VO_x species and polymeric VO_x species as reported in the previous literature [7,12,13,26]. However, the correspondence between these bands and the V–O bond species remains controversial. To clarify the attribution of the vibrational bands to the V–O bonds, we calculated the Raman spectra of the three VO_x configurations using the DFT method (detailed in Table S5). It can be found that there is a significant linear correlation between the bond lengths and the Raman vibrational frequency (see Fig. S7 for detailed linear relationships). The band at about 1020 cm^{-1} corresponds to the vibration of the terminal V=O bond and those at 1000 and 955 cm^{-1} to the two bonds of the terminal $V(=O)_2$ bond. The bond length of $V(=O)_2$ is longer than that of V=O, causing the corresponding vibrational frequency shift to lower. They fit well to the bands at 1030 and 930 cm^{-1} (and a weak shoulder peak at 1000 cm^{-1}) in the experimental Raman spectra within a certain error. This also provides evidence for the existence of the $V(=O)_2$ structure, which is representative of the polymeric VO_x species. Notably, the band at 930 cm^{-1} was not observed until the sample had a V_2O_5 loading of 2%. It can be matched with the variation in the number of Polymers in the random calculation.

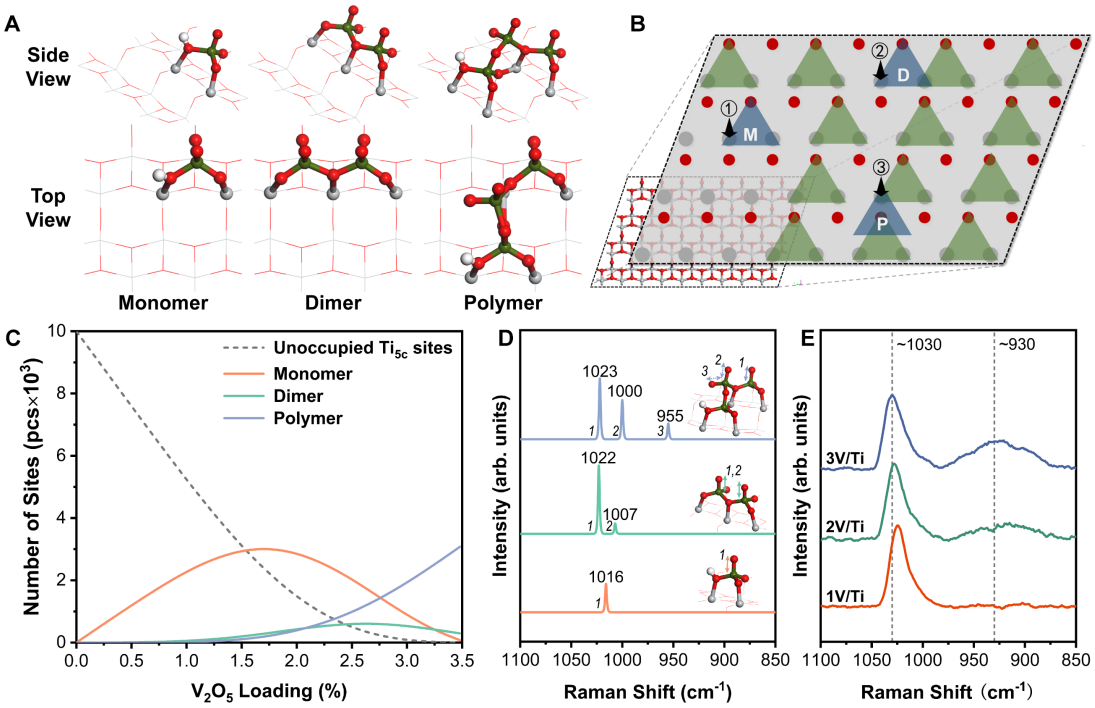

Fig. 1. Structure and distribution of VO_x active sites. (A) Optimized structures of the Monomer, Dimer, and Polymer active sites on anatase TiO_2 (101) surface. Vanadium in green, titanium in gray, oxygen in red, and hydrogen in white. **(B)** Schematic diagram of the restricted random distribution model of sites. Gray dots, red dots, and triangles represent Ti_{5c}, O_{2c}, and loaded VO_x (M–Monomer, D–Dimer, P–Polymer), respectively. **(C)** Variation curves of the number of different VO_x active sites with V_2O_5 loading, calculated by the random distribution model. **(D and E)** Raman spectra obtained by **(D)** DFT calculation (for VO_x sites) and **(E)** experiment (for catalyst samples).

3.2. NH_3 adsorption properties on the acid sites of VO_x

It is well known that the occurrence of the NH_3-SCR reaction first requires the adsorption of NH_3 on acid sites of the catalyst, including Brønsted acid (B-acid) sites and Lewis acid (L-acid) sites. To elucidate the acid site characteristics of different VO_x configurations (corresponding to different V loadings samples), we conducted diffuse reflectance infrared Fourier transform spectroscopy (DRIFTS) (Fig. 2A) and NH_3 temperature programmed desorption (NH_3-TPD) (Fig. 2C) studies. The NH_3 adsorption energy using DFT methods was calculated as a supplement. With these, we can provide more evidence of the correspondence between the DFT configuration and the real catalyst.

In situ DRIFTS was employed to investigate the changes of NH_3 adsorption at two acid sites in different samples. The DRIFTS spectra of stable NH_3 adsorption are shown in Fig. 2A (see Fig. S8 for the spectrum of the pure TiO_2 sample). The band at about 1200 and 1420 cm^{-1} were attributed to the NH_3 adsorbed on the L-acid and NH_4^+ adsorbed on the B-acid, respectively. The integrated area of the peaks can qualitatively represent the number of acid sites. With the increase of vanadia loading, the amount of B-acid increases linearly from very little, proving that it originates from VO_x species. In contrast, the amount of L-acid shows a gradually decreasing trend. It was reported that both Ti and V sites exposed on the surface could serve as L-acid sites [30]. This decreasing trend may be attributed to the occupation and replacement of Ti L-acid sites by V L-acid sites and the weaker IR signal of V L-acid sites. Meanwhile, the IR sensitivities of these two bands are uncertain under different conditions [30,41], so it is unreliable to use the band absolute intensity ratios to compare the amount of two kinds of adsorbed NH_3.

To make the DFT calculation correspond to the condition of exposure to the NH_3 atmosphere during NH_3 adsorption, we first calculated the possibility of surface hydrogenation of the VO_x structures. The hydrogenation energy was defined as Eqs. S7 and S8. Hydrogenation sites are on the terminal oxygen corresponding to each V atom. Fig. 2B shows that the hydrogenation free energy of all VO_x configurations (Monomer, Dimer, and Polymer) is less than zero within the experimental temperature range (300 K ~ 800 K) under NH_3 exposure conditions. It implies that they all tend to be hydrogenated. As mentioned in the previous section, the formation of Dimer and Polymer will be accompanied by consumption of −OH, which contradicts the increasing trend of B-acid in DRIFTS. However, enough −OH sites can be further provided under the NH_3 atmosphere in a hydrogenation way, which can explain the increase in the amount of B-acid.

The results of NH_3 adsorption energy (calculated by Eq. S9) by DFT calculations and the NH_3-TPD curves by experiments were compared in Fig. 2C. In the calculation part, typical B-acid sites and L-acid sites on the Monomer, Dimer, and Polymer were considered. The hydrogenated configurations were employed to correspond to the NH_3

exposure condition. From the NH_3-TPD results, we found that all the curves generally exhibit a broad peak from 100 °C to 500 °C, representing the diversity and complexity of NH_3 adsorption species. Specifically, with the increase of V loading, the area of the high-temperature desorption peaks gradually decreased, whereas the area of the low-temperature peaks increased (see Fig. S9 for the NH_3-TPD profile of the pure TiO_2 sample). Combined with the NH_3 adsorption energy data, it can be speculated that the high-temperature desorption peak mainly corresponds to the NH_3 species adsorbed on Ti L-acid sites (a), which has the highest adsorption energy. For higher V loading, the adsorption sites of NH_3 gradually changed from Ti L-acid to VO_x B-acid and L-acid (b and c). Their lower adsorption energies increase the experimental low-temperature desorption peak area. In addition, physically weakly adsorbed NH_3 (d) exists in various cases and can correspond to low-temperature peaks with common features in the TPD curve.

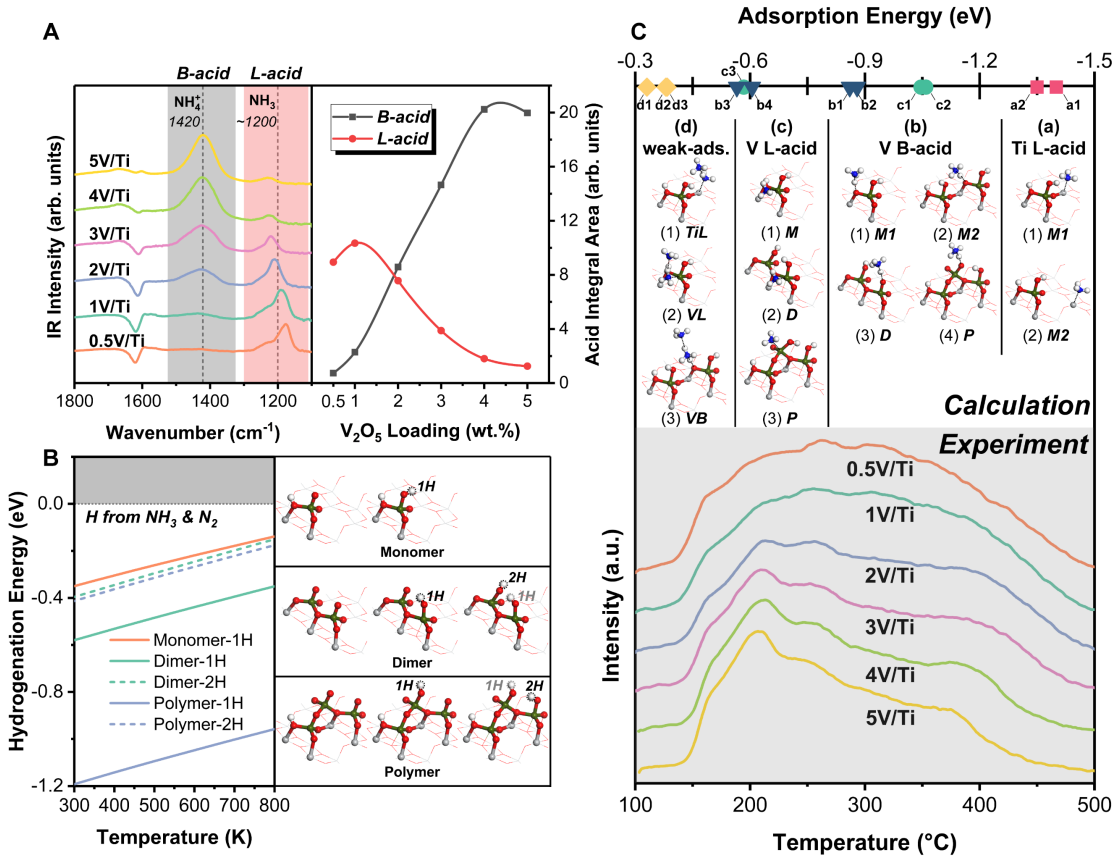

Fig. 2. NH_3 adsorption characteristics of the acid sites. (A) *In situ* DRIFTS spectra of stable NH_3 saturated adsorption (left) and integrated area of the characteristic peaks at 1200 cm^{-1} and 1420 cm^{-1} (right), with the variation of V_2O_5 loading. Note:

The background spectrum of samples was collected in the N_2 atmosphere. All samples were exposed to NH_3 (500 ppm) at 200 °C until saturated adsorption. **(B)** Calculated hydrogenation energy of different VO_x active sites in NH_3 atmosphere. **(C)** Correspondence between calculated NH_3 adsorption energy (top) and NH_3-TPD results (bottom).

3.3. NH_3-SCR reactivity of the VO_x active sites

We start by focusing on the intrinsic reactivity (TOF) of the catalyst for NH_3-SCR to obtain the basic law of reaction kinetics. Fig. 3A exhibits the variation of TOF with V_2O_5 loading at different temperatures. It shows that in a certain temperature range, TOF has an apparent upward trend with the increase of V loading. With the help of the relationship between V loading and active site structures mentioned above, we can infer that the improvement of TOF is mainly attributed to the morphological transformation of VO_x sites. The decrease of TOF at higher temperatures (> 400 °C) and higher V_2O_5 loading (> 3~4 wt.%) may be due to the direct oxidation of NH_3 and excessive coverage of active sites.

To further explain such activity enhancement, we investigated the reactivity of adsorbed NH_3 using *in situ* DRIFTS to illustrate the role of L-acid and B-acid sites in this process. The spectra of the consumption of adsorbed NH_3 by reacting with NO and O_2 are displayed in Fig. S10. For data comparability, relative consumption was obtained by peak area normalization, shown in Figs. 3B and 3C. In this analysis, we exclude the data of 4V/Ti, 5V/Ti in the L-acid part, and 0.5V/Ti, 1V/Ti in the B-acid part, whose too small peak area leads to a large error. It can be seen that the NH_3 species adsorbed on L-acid and B-acid sites were consumed with time, indicating that they were both involved in the reaction. In addition, both adsorbed NH_3 species exhibited an upward trend in terms of the average consumption rates with the increase of V loading. Here, the average consumption rate was calculated from the first half of the consumption and the corresponding time used. It is consistent with the regularity shown by the TOF data. Notably, there is a lag in the consumption rate of NH_3 species adsorbed on the B-acid sites in the first few minutes compared with L-acid sites. Over time, the two will gradually reach the same level. The

282 comparison of the intrinsic reactivity of L-acid and B-acid sites remains controversial, which involves the
283 transformation of acid sites and the migration of NH_3 reaction sites [30,41–44].

284 In order to elucidate the mechanism underlying the catalytic reactivity difference between the Monomer, Dimer,
285 and Polymer at the atomic scale, DFT calculations were performed. Typical L-acid and B-acid sites on different
286 VO_x sites were involved during the calculation, whose detailed energies (the free energies at 0K and 298K) and
287 structures in the reaction pathways are shown in Figs. 3D (Monomer&Ti L-acid site) and S11 (other sites). The
288 general agreement is that the complete cycle of NH_3-SCR consists of reduction and reoxidation processes.
289 Referring to previous literatures [24,26,32], the beginning of our mechanism is the formation of the NH_2NO
290 intermediate from the reaction of adsorbed NH_3 and weakly adsorbed NO (Eley–Rideal mechanism) on the VO_x
291 sites (A→E, G→K). Then, the NH_2NO intermediate is desorbed and decomposed into N_2 and H_2O (E→G, K→
292 M). Two consecutive additions of NH_3 will lead to the formation of H_2O, which can be removed from the surface
293 (M). The transition state (D and J, denoted TS1 and TS2) is characterized by the breaking of the N−H bond with
294 the participation of NO, followed by the transfer of H ions to VO_x sites. After the above reduction process, the
295 subsequent addition of O_2 was employed for the reoxidation. Actually, the reaction stoichiometry dictates the
296 reoxidation process requires two more NH_3 to complete the catalyst cycle (M→A, shown in Fig. S11B). We found
297 that the barrier in the reoxidation process is smaller than in the reduction process (Figs. 3D and S11B). This is in
298 agreement with the experiment results of Zhu et al. [31] that the rate of reoxidation is significantly faster than the
299 reduction, indicating that the reduction process is the rate-determining step of the total reaction cycle. Therefore,
300 only the reduction process was involved in the following study, whose energy barrier was regarded as the descriptor
301 of overall reactivity. In addition, the V=O group was employed as the redox site for the reaction, which is more
302 advantageous due to its lower reaction energy barrier compared to the V−O−Ti site (Figs. 3D and S11M). Notably,
303 due to the oxidizing atmosphere in the SCR reaction, V^{5+} sites were regarded as the cycle start in the majority.

304 However, reduced V^{4+} sites are generated at some point in the reaction path, which can provide some extra B-acid
305 sites [32].

306 The decisive energy barrier of transition states (the larger of TS1 and TS2, the free energy at 298 K) of all VO_x
307 active sites involved are exhibited in Figs. 3E and 3F. These sites were further distinguished into single and dual
308 sites depending on whether the NH_3 adsorption and redox occurred at one single vanadium site. By comparing
309 these energy barriers, we can draw the following conclusions. First, the Monomer has a large energy barrier when
310 it functions as a single site, including its L-acid and B-acid sites, implying particularly poor reactivity. When it
311 forms dual sites with the Ti L-acid site (denoted as Monomer&Ti), the barrier decreases to a certain extent. It
312 suggests that the Monomer&Ti site plays a major role in low V loading catalyst dominated by isolated Monomer,
313 while the activity is still lacking. With the gradual increase of monomer density, the adjacent monomer pairs
314 (represented as adj-Monomer) appear and provide the dual site. The energy barrier involving its L-acid is similar
315 to the Monomer&Ti site, while that involving the B-acid becomes lower significantly. In addition, the Dimer and
316 Polymer can also form similar dual sites (denoted as DimerD and PolymerD), which involve the B-acid of the
317 Dimer and the L-acid and B-acid of the Polymer. These sites all exhibit even lower energy barriers, reflecting the
318 great positive effect of dual sites on the reaction. It is also consistent with the conclusion in previous literature that
319 the SCR reaction involves two vanadium sites or oligomeric vanadium on the surface [17,26,28]. Remarkably, the
320 Polymer shows a more obvious enhancement effect on the activity than the Monomer and Dimer. Even the single
321 site formed by it also exhibits a considerably low barrier. We speculate that it is due to the role of the terminal
322 $V(=O)_2$ bond of the Polymer as a redox site. According to the calculation model, it can be found that the terminal
323 $V(=O)_2$ bond has better structural flexibility in the reaction process than the V=O bond, which is more conducive
324 to the transfer of H ion in the redox process, thereby reducing the energy barrier. It is worth noting that the reaction
325 barrier of B-acid sites is overall lower than that of L-acid sites in the calculated results, suggesting that the B-acid

site may be more dominant in the reaction. However, the experimental results in Figs. 3B and 3C show similar reactivity between the two. Regarding the difference between the two, one possible reason is that the NH_3 adsorbed on L-acid sites may migrate to the adjacent B-acid site for reaction, and another speculation is that part of the B-acid sites may be transformed from the L-site. They all may level out the reaction rate of L-acid and B-acid exhibited in the actual reaction process. In general, the above discussion indicates that both factors of the dual sites and the terminal $V(=O)_2$ affect the SCR reactivity through structural effects rather than electronic effects [17]. This conclusion can be supported by the fact that the different samples exhibit the similar position of reduction peaks in the TPR results (shown in Fig. S12).

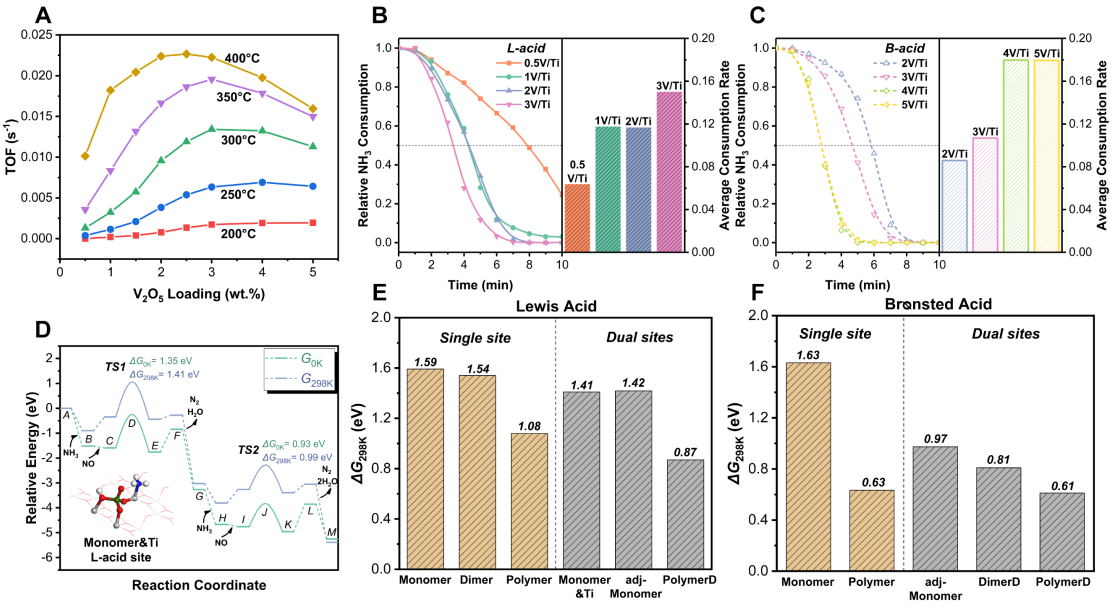

Fig. 3. SCR reactivity properties. (A) Variation of measured TOF with the V_2O_5 loading and temperature. **(B and C)** *In situ* DRIFTS results of relative NH_3 consumption for reaction with NO + O_2 and corresponding average consumption rates (calculated by half-consumption) on **(B)** L-acid sites and **(C)** B-acid sites with the variation of V_2O_5 loading. **(D)** Calculated energy profile for reduction process of NH_3-SCR reaction over Monomer&Ti L-acid site. The values of the energy barrier are highlighted. The green and blue lines represent the free energy at 0 K and 298 K, respectively. The letters at each state correspond to the detailed structures in Fig. S11A. **(E and F)** Decisive energy barriers of different VO_x active sites, distinguished by **(E)** L-acid and **(F)** B-acid. The involved structures are shown in Fig. S11.

342 *3.4. Validation of the theoretical model*

343 Above, we discussed the experimental phenomenon and the calculation results regarding reactivity enhancement.
344 To further investigate the consistency between the two aspects, we compared the reaction activation energies
345 obtained from experiments and calculations, which were treated as the characteristic indicator.

346 As for the calculated activation energy, the contribution of each kind of VO_x site to the activation energy needs
347 to be comprehensively considered. An average calculated activation energy (denoted as Ea_c) was obtained by the
348 following formula:

349 $$Ea_c = -RT \ln(\sum_{n}^{i} c_i \exp(\frac{-\Delta G_i}{RT})) \quad (2)$$

350 where the c_i *and* ΔG_i represent the numerical proportions of different VO_x sites and their energy barrier,
351 respectively. The proportions were obtained by normalizing the absolute number from the random distribution
352 result in Section 3.1, involving the Monomer (distinguishing isolated and adjacent), Dimer, and Polymer, as shown
353 in Figs. 4A and 4B. The lowest energy barrier corresponding to each kind of VO_x site was employed for the
354 calculation, which is reasonable since it can represent the dominant reaction path of the site. The temperature T
355 was set to 298 K, consistent with the temperature condition of ΔG_i. On the other hand, to determine the
356 experimental activation energy for the reaction, the rate constant must be obtained first. It can be assumed that the
357 reaction is first-order in NO partial pressure and zeroth-order in NH_3 partial pressure. With the large excess of O_2,
358 the reaction rate can be regarded as pseudo-first-order [7]. Then the rate constant can be written as Eq. S3. The
359 experimental activation energy (denoted as Ea_e) was determined from the slope by the Arrhenius plots of ln k
360 versus 1000/T, shown in Fig. S13.

361 The results of the Ea_c and the Ea_e were given in Fig. 4C and compared (see Table S6 for detailed data). We
362 found that both the calculated and experimental values show a downward trend with the increase of V loading,
363 which explains the enhancement of reactivity from the perspective of activation energy. Specifically, with the V

loading from 0.5% to 3%, Ea_c decreases from 0.83 eV to 0.63 eV, while Ea_e decreases from 0.70 eV to 0.43 eV. There is a deviation of 0.13 – 0.20 eV in absolute value between Ea_c and Ea_e, which may be due to the inherent error from the computational model. However, their relative decreasing trend is in good agreement (both decline by about 0.2 eV). This provides strong evidence for the consistency and comparability between the experimental and computational results and also indicates that the random distribution model is quite feasible as a quantitative link.

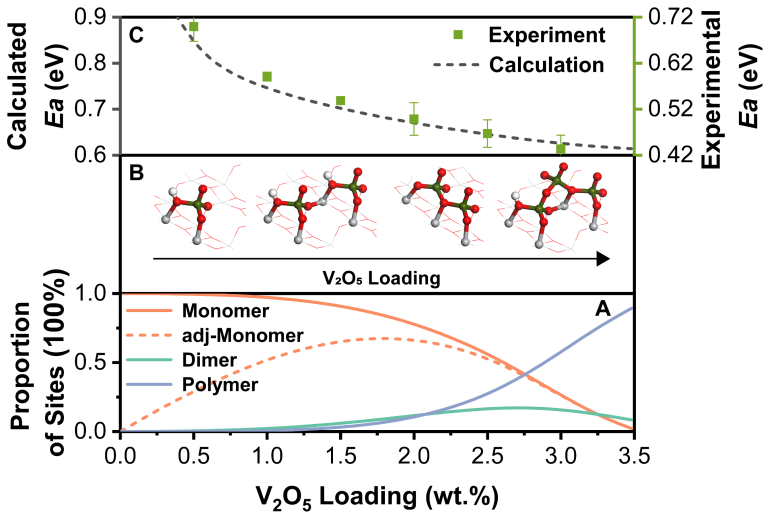

Fig. 4. Results of reaction activation energy. (A) Number proportions of different VO_x active sites with the variation of V_2O_5 loading based on the random distribution theory. **(B)** Schematic diagram of the relationship between active site structure and V_2O_5 loading. **(C)** Comparison between calculated and experimental values of reaction activation energy.

4. Conclusion

This study has presented a validated strategy to assess the effect of active site morphology on reactivity. The most stable structures of VO_x active sites on TiO_2 support were determined by DFT calculation. The restricted random distribution model of active sites was proposed, which clearly relates the vanadia loading to the configurations of active sites (Monomer, Dimer, and Polymer) and their number distribution, integrating the experiment with the DFT calculation closely. The results of this work revealed the essence of the progressive

enhancement in SCR reactivity (TOF) with increasing vanadia loading. From the calculations of reaction pathways, this enhancement is mainly attributed to the formation of the dual sites and the terminal $V(=O)_2$ bond, which originate from the adjacent and aggregated VO_x sites. A good match between the experimental and calculated values of the reaction activation energy verified the validation of this theoretical model. These new insights advance the understanding of the nature of the active sites and the working mechanism of metal oxide catalysts, which can serve as a guide to optimize the metal oxide–metal oxide interaction for future catalyst design.

CRediT authorship contribution statement

Jingyu Xue: Methodology, Investigation, Formal analysis, Visualization, Writing – Original Draft. **Yang Zhang:** Supervision, Writing – Review & Editing. **Wenshuo Hu:** Supervision, Writing – Review & Editing. **Yanrong Chen:** Supervision, Writing – Review & Editing. **Zhongqing Yang:** Supervision, Resources. **Jingyu Ran:** Supervision, Resources. **Xinbao Li:** Resources. **Xin Tu:** Supervision, Writing – Review & Editing. **Xuesen Du:** Conceptualization, Supervision, Methodology, Formal analysis, Writing – Review & Editing.

Declaration of Competing Interest

The authors declare that they have no known competing financial interests or personal relationships that could have appeared to influence the work reported in this paper.

Data availability

Data will be made available on request.

Acknowledgements

We thank Prof. William F. Schneider of the University of Notre Dame for providing the inspiration on the original model and valuable advice on the format and text of the earlier manuscript. We also thank Dr. Yujia Wang of the University of Notre Dame for the technical guidance and assistance in building the theoretical model. We

gratefully acknowledge the financial support from the National Natural Science Foundation of China (52176100), National Key R&D Program of China (2021YFE0110800), Natural Science Foundation of Chongqing (cstc2021jcyj-msxmX0247), and Open Fund of Guangdong Province Engineering Laboratory for Air Pollution Control (20193236-09-02).

Appendix A. Supplementary data

Supplementary data associated with this article can be found in the online version.

References

[1] Bañares MA, Wachs IE. Molecular structures of supported metal oxide catalysts under different environments. J Raman Spectrosc 2002;33(5):359–80.

[2] van Deelen TW, Hernández Mejía C, de Jong KP. Control of metal-support interactions in heterogeneous catalysts to enhance activity and selectivity. Nat Catal 2019;2(11):955–70.

[3] Lin S, Li Z, Li M. Tailoring metal-support interactions via tuning CeO_2 particle size for enhancing CO_2 methanation activity over Ni/CeO_2 catalysts. Fuel 2023;333:126369.

[4] Arena F, Giordano N, Parmaliana A. Working Mechanism of Oxide Catalysts in the Partial Oxidation of Methane to Formaldehyde. II. Redox Properties and Reactivity of SiO_2, MoO_3/SiO_2, V_2O_5/SiO_2, TiO_2, and V_2O_5/TiO_2 Systems. J Catal 1997;167(1):66–76.

[5] Kaichev VV, Chesalov YA, Saraev AA, Klyushin AY, Knop-Gericke A, Andrushkevich TV, Bukhtiyarov VI. Redox mechanism for selective oxidation of ethanol over monolayer V_2O_5/TiO_2 catalysts. J Catal 2016;338:82–93.

[6] Kamata H, Ohara H, Takahashi K, Yukimura A, Seo Y. SO_2 oxidation over the V_2O_5/TiO_2 SCR catalyst. Catal Lett 2001;73(1):79–83.

[7] Lai J-K, Wachs IE. A Perspective on the Selective Catalytic Reduction (SCR) of NO with NH_3 by Supported V_2O_5–WO_3/TiO_2 Catalysts. ACS Catal 2018;8(7):6537–51.

[8] Younas U, Ahmad A, Islam A, Ali F, Pervaiz M, Saleem A, Waseem M, Muteb Aljuwayid A, Habila MA, Raza Naqvi S. Fabrication of a novel nanocomposite (TiO_2/WO_3/V_2O_5) by hydrothermal method as catalyst for hazardous waste treatment. Fuel 2023;349:128668.

[9] Went GT, Oyama ST, Bell AT. Laser Raman spectroscopy of supported vanadium oxide catalysts. J Phys Chem 1990;94(10):4240–6.

[10] Vuurman MA, Wachs IE, Hirt AM. Structural determination of supported V_2O_5–WO_3/TiO_2 catalysts by *in situ* Raman spectroscopy and x-ray photoelectron spectroscopy. J Phys Chem 1991;95(24):9928–37.

[11] Amiridis MD, Wachs IE, Deo G, Jehng J-M, Kim DS. Reactivity of V_2O_5 Catalysts for the Selective Catalytic Reduction of NO by NH_3: Influence of Vanadia Loading, H_2O, and SO_2. J Catal 1996:161(1):247–53.

[12] Wachs IE. Catalysis science of supported vanadium oxide catalysts. Dalton Trans 2013;42(33):11762–9.

[13] Ganjkhanlou Y, Janssens TVW, Vennestrøm PNR, Mino L, Paganini MC, Signorile M, Bordiga S, Berlier G. Location and activity of VO_x species on TiO_2 particles for NH_3-SCR catalysis. Appl Catal B 2020;278:119337.

[14] Nuguid RJG, Ferri D, Marberger A, Nachtegaal M, Kröcher O. Modulated Excitation Raman Spectroscopy of V_2O_5/TiO_2: Mechanistic Insights into the Selective Catalytic Reduction of NO by NH_3. ACS Catal 2019;9:6814–20.

[15] Eckert H, Wachs IE. Solid-state ^{51}V NMR structural studies on supported vanadium(V) oxide catalysts: vanadium oxide surface layers on alumina and titania supports. J Phys Chem 1989;93(18):6796–805.

[16] Hu JZ, Xu S, Li W-Z, Hu MY, Deng X, Dixon DA, Vasiliu M, Craciun R, Wang Y, Bao X, Peden CHF. Investigation of the Structure and Active Sites of TiO_2 Nanorod Supported VO_x Catalysts by High-Field and Fast-Spinning ^{51}V MAS NMR. ACS Catal 2015;5(7):3945–52.

[17] Jaegers NR, Lai J-K, He Y, Walter E, Dixon DA, Vasiliu M, Chen Y, Wang C, Hu MY, Mueller KT, Wachs IE, Wang Y, Hu JZ. Mechanism by which Tungsten Oxide Promotes the Activity of Supported V_2O_5/TiO_2 Catalysts for NO_x Abatement: Structural Effects Revealed by ^{51}V MAS NMR Spectroscopy. Angew Chem Int Ed 2019;58(36):12609–16.

[18] Centeno MA, Malet P, Carrizosa I, Odriozola JA. Lanthanide Doped V_2O_5/Al_2O_3 Catalysts: Structure–Activity Relationship in the SCR of NO_x. J Phys Chem B 2000;104(14):3310–9.

[19] Anpo M, Higashimoto S, Matsuoka M, Zhanpeisov N, Shioya Y, Dzwigaj S, Che M. The effect of the framework structure on the chemical properties of the vanadium oxide species incorporated within zeolites. Catal Today 2003;78(1–4):211–7.

[20] Rodella CB, Mastelaro VR. Structural characterization of the V_2O_5/TiO_2 system obtained by the sol–gel method. J Phys Chem Solids 2003;64(5):833–9.

[21] Vining WC, Goodrow A, Strunk J, Bell AT. An experimental and theoretical investigation of the structure and reactivity of bilayered $VO_x/TiO_x/SiO_2$ catalysts for methanol oxidation. J Catal 2010;270(1):163–71.

[22] Arnarson L, Rasmussen SB, Falsig H, Lauritsen JV, Moses PG. Coexistence of Square Pyramidal Structures of Oxo Vanadium (+5) and (+4) Species Over Low-Coverage VO_x/TiO_2 (101) and (001) Anatase Catalysts. J Phys Chem C 2015;119(41):23445–52.

[23] Arnarson L, Falsig H, Rasmussen SB, Lauritsen JV, Moses PG. The reaction mechanism for the SCR process on monomer V^{5+} sites and the effect of modified Brønsted acidity. Phys Chem Chem Phys 2016;18(25):17071–80.

[24] Arnarson L, Falsig H, Rasmussen SB, Lauritsen JV, Moses PG. A complete reaction mechanism for standard and fast selective catalytic reduction of nitrogen oxides on low coverage VO_x/TiO_2 (001) catalysts. J Catal 2017;346:188–97.

[25] Song I, Lee J, Lee G, Han JW, Kim DH. Chemisorption of NH_3 on Monomeric Vanadium Oxide Supported on Anatase TiO_2: A Combined DRIFT and DFT Study. J Phys Chem C 2018;122(29):16674–82.

[26] He G, Lian Z, Yu Y, Yang Y, Liu K, Shi X, Yan Z, Shan W, He H. Polymeric vanadyl species determine the low-temperature activity of V-based catalysts for the SCR of NO_x with NH_3. Sci Adv 2018;4(11):eaau4637.

[27] Ramis G, Busca G, Bregani F, Forzatti P. Fourier transform-infrared study of the adsorption and coadsorption of nitric oxide, nitrogen dioxide and ammonia on vanadia–titania and mechanism of selective catalytic reduction. Appl Catal 1990;64:259–78.

[28] Topsøe NY. Mechanism of the selective catalytic reduction of nitric oxide by ammonia elucidated by *in situ* on-line fourier transform infrared spectroscopy. Science 1994;265(5176):1217–9.

[29] Topsøe NY, Topsøe H, Dumesic JA. Vanadia/Titania Catalysts for Selective Catalytic Reduction (SCR) of Nitric Oxide by Ammonia. J Catal 1995;151(1):226–40.

[30] Zhu M, Lai J-K, Tumuluri U, Wu Z, Wachs IE. Nature of Active Sites and Surface Intermediates during SCR of NO with NH_3 by Supported V_2O_5–WO_3/TiO_2 Catalysts. J Am Chem Soc 2017;139(44):15624–7.

[31] Zhu M, Lai J-K, Tumuluri U, Ford ME, Wu Z, Wachs IE. Reaction Pathways and Kinetics for Selective Catalytic Reduction (SCR) of Acidic NO_x Emissions from Power Plants with NH_3. ACS Catal 2017;7(12):8358–61.

[32] Mason MM, Lee ZR, Vasiliu M, Wachs IE, Dixon DA. Initial Steps in the Selective Catalytic Reduction of NO with NH_3 by TiO_2-Supported Vanadium Oxides. ACS Catal 2020;10(23):13918–31.

[33] Perdew JP, Burke K, Ernzerhof M. Generalized Gradient Approximation Made Simple. Phys Rev Lett 1996;77(18):3865–8.

[34] Grimme S, Antony J, Ehrlich S, Krieg H. A consistent and accurate *ab initio* parametrization of density functional dispersion correction (DFT-D) for the 94 elements H–Pu. J Chem Phys 2010;132(15):154104.

[35] Peng Y, Si W, Li X, Luo J, Li J, Crittenden J, Hao J. Comparison of MoO_3 and WO_3 on arsenic poisoning V_2O_5/TiO_2 catalyst: DRIFTS and DFT study. Appl Catal B 2016;181:692–8.

[36] Das T, Tosoni S, Pacchioni G. Layered oxides as cathode materials for beyond-Li batteries: A computational study of Ca and Al intercalation in bulk V_2O_5 and MoO_3. Comput Mater Sci 2021;191:110324.

[37] Sheppard D, Xiao P, Chemelewski W, Johnson DD, Henkelman G. A generalized solid-state nudged elastic band method. J Chem Phys 2012;136(7):074103.

[38] Sun C, Liu L-M, Selloni A, Lu GQ, Smith SC. Titania–water interactions: a review of theoretical studies. J Mater Chem 2010;20(46):10319–34.

[39] Howard CJ, Sabine TM, Dickson F. Structural and thermal parameters for rutile and anatase. Acta Crystallogr Sect B Struct Sci 1991;47(4):462–8.

[40] Lazzeri M, Vittadini A, Selloni A. Structure and energetics of stoichiometric TiO_2 anatase surfaces. Phys Rev B 2001;63(15):155409.

[41] Song I, Lee H, Jeon SW, Kim T, Kim DH. Time-resolved observation of V_2O_5/TiO_2 in NH_3-SCR reveals the equivalence of Brønsted and Lewis acid sites. Chem Commun 2020;56(98):15450–3.

[42] Due-Hansen J, Rasmussen SB, Mikolajska E, Bañares MA, Ávila P, Fehrmann R. Redox behaviour of vanadium during hydrogen–oxygen exposure of the V_2O_5–WO_3/TiO_2 SCR catalyst at 250 °C. Appl Catal B 2011;107(3–4):340–6.

[43] Marberger A, Ferri D, Elsener M, Kröcher O. The Significance of Lewis Acid Sites for the Selective Catalytic Reduction of Nitric Oxide on Vanadium-Based Catalysts. Angew Chem Int Ed 2016;55(39):11989–94.

[44] Xu G, Li H, Yu Y, He H. Dynamic Change of Active Sites of Supported Vanadia Catalysts for Selective Catalytic Reduction of Nitrogen Oxides. Environ Sci Technol 2022;56(6):3710–8.